Biophysical Reports

ARTICLE

Viro-fluidics: Real-time analysis of virus production kinetics at the single-cell level

Joëlle Eid,[1] Marius Socol,[1,*] Antoine Naillon,[2] Jérôme Feuillard,[1] Luca Ciandrini,[3] Emmanuel Margeat,[3] Benoit Charlot,[4] and Marylène Mougel[1,*]

[1]Team R2D2: Retroviral RNA Dynamics and Delivery, IRIM, UMR9004, CNRS, University of Montpellier, Montpellier, France; [2]Université Grenoble Alpes, CNRS, Grenoble INP, 3SR, Grenoble, France; [3]CBS, Université de Montpellier, CNRS, INSERM, Montpellier, France; and [4]IES, Université de Montpellier, CNRS, Montpellier, France

ABSTRACT Real-time visualization and quantification of viruses released by a cell are crucial to further decipher infection processes. Kinetics studies at the single-cell level will circumvent the limitations of bulk assays with asynchronous virus replication. We have implemented a "viro-fluidic" method, which combines microfluidics and virology at single-cell and single-virus resolutions. As an experimental model, we used standard cell lines producing fluorescent HIV-like particles (VLPs). First, to scale the strategy to the single-cell level, we validated a sensitive flow virometry system to detect VLPs in low concentration samples ($\geq 10^4$ VLPs/mL). Then, this system was coupled to a single-cell trapping device to monitor in real-time the VLPs released, one at a time, from single cells under cell culture conditions. Our results revealed an average production rate of 50 VLPs/h/cell similar to the rate estimated for the same cells grown in population. Thus, the virus-producing capacities of the trapped cells were preserved and its real-time monitoring was accurate. Moreover, single-cell analysis revealed a release of VLPs with stochastic bursts with typical time intervals of few minutes, revealing the existence of limiting step(s) in the virus biogenesis process. Our tools can be applied to other pathogens or to extracellular vesicles to elucidate the dissemination mechanisms of these biological nanoparticles.

WHY IT MATTERS We are frequently exposed to viruses, but some of them, like HIV, cause fatal diseases and pandemics. We have developed a simple viro-fluidic system that requires only fluorescent labeling of viral particles and allows direct observation of viruses exiting a cell, one by one, under cell culture conditions. The system operates in real-time and at single-cell and single-viral particle resolutions. Our results reveal HIV production at a moderate frequency that was not predicted for optimal virus dissemination. Importantly, the viro-fluidic tool is remarkably easy for biologists to access and is transposable to other pathogens or extracellular vesicles.

INTRODUCTION

The development of hydrodynamic-based microfluidic biochips has revolutionized biology and the fields of health sciences by enabling studies at the single-cell scale (1–3). It has also greatly contributed to the recent development of single-cell virology (for a review see (4,5)). A large panel of strategies has been developed based on microwells, microvalves, and droplets for studying viral infection at the single-cell level. Typically, droplets have been applied to high-throughput screening (6–9), and microwell- and valve-based technologies to multiparameter analysis and infection dynamics analysis (10–12).

In the field of the human immunodeficiency virus type 1 (HIV-1), responsible for the acquired immunodeficiency syndrome pandemic, the microfluidics has been mainly used for the diagnostics of acquired immunodeficiency syndrome with the detection of viral nucleic acids or anti-HIV antibodies (13), and for high-throughput screening of therapeutic tests (14–16) or transcriptome analysis (17–19) (for a review see (20)). Here, we implemented a "viro-fluidics" approach that combines continuous microfluidics using chips fabricated from polydimethylsiloxane (PDMS) and virology under cell culture conditions. Our goal is to study the real-time kinetics of virus production, masked by bulk assays, through uninterrupted single-cell

Submitted May 12, 2022, and accepted for publication August 5, 2022.

*Correspondence: marius.socol@irim.cnrs.fr or marylene.mougel@irim.cnrs.fr

Editor: Jorg Enderlein.

https://doi.org/10.1016/j.bpr.2022.100068

culture and continuous single-virus imaging. As a proof of concept, we applied viro-fluidics to study the release of HIV-1 VLPs from a model cell system, which does not require BL3 safety practices.

The biogenesis of HIV-1 in cell is well documented (for review see (21)), including late steps such as virus assembly at, and budding from, the plasma membrane. These late stages are driven by the structural polyprotein Gag, which has the ability to self-assemble by thousands and release VLPs with the native conformation of the virus but without genetic material (22,23). This is why VLPs are commonly used as an experimental model to study the late steps of HIV biogenesis. In addition, the study of VLP production is also relevant for vaccination strategies, as these noninfectious particles are promising platforms for vaccine candidates due to their potential to generate high immunogenic responses with few side effects (24). Assembly and budding events are frequently studied in human HeLa or HEK293 cellular models expressing labeled HIV Gag, mainly using advanced live cell fluorescence imaging techniques (25–30). However, the final step of virus release into the extracellular space, crucial for understanding the mechanisms of virus production and virus-host interplay, remains incompletely deciphered. Studying cell populations with heterogeneous HIV-1 replication kinetics would provide global and approximate data. An approach is therefore needed at the single-cell level to address the dynamics of virus release and provide information on the amount of virus produced, the production rate, and the frequency, as well as the heterogeneity of virus production between cells. The system must also allow visualization and quantification of individual VLPs with high sensitivity, since VLPs exiting a single cell are at low concentration with stochastic occurrence in the culture medium flow. VLP fluorescence guarantees the specificity of the detected signals and avoids contamination with the numerous cellular vesicles also released by the cell (EVs).

First, we set up a virometry device specifically designed to detect individual fluorescent VLPs in flow. Its performances were tested by a commercial device: nanoparticle tracking analysis (NTA) (30,31). The remarkable simplicity of our flow virometry system makes it a useful and inexpensive tool for virologists who need to detect and quantify viral particles directly in a biological sample (without a concentration step). We then integrated this tool downstream of a single-cell trapping microfluidic device to visualize each VLP produced by a single living cell and released into the flow. The chip operated at different scales of analysis (micro- and nanometric) with cells of about 15 μm and VLPs of about 140 nm in diameter (visualized with a 40$\times$ objective). This viro-fluidic chip was able to capture and immobilize single cells in a flow without damage, maintain the cells trapped and perfused for several hours without apoptosis/necrosis, and detect and quantify each VLP released one at a time from the single cell. Cellular abilities to produce virions were not disturbed by the microfluidic system since similar production rates were found in population-scale experiments performed with the same cells concomitantly. The viro-fluidics tool provided access to the dynamics of HIV production and revealed that production occurred at a rate of tens of VLPs per hour. This did not increase gradually over time as first suspected, but followed a release mechanism with a typical kinetics, suggesting that one or more limiting steps regulate the virus formation mechanism.

MATERIALS AND METHODS

Cell lines producing fluorescent VLPs

Stable human cell lines HeLa (17 $\pm$ 5 μm) or HEK293 (13 $\pm$ 4 μm) that produce HIV noninfectious fluorescent VLPs were established. Cells were cultured in medium with or without phenol red (F12) and supplemented with 10% fetal bovine serum at 37°C and 5% CO_2. They were transfected with a plasmid expressing HIV-1 Gag protein fused to GFP and carrying a positive selection marker (geneticin resistance) by using JetPEI reagent (Polyplus, Strasbourg, France), as described previously (32) (Fig. 1). Two days after transfection, the cells were treated with geneticin G418 and, after 2 weeks, fluorescent G418-resistant transfected cells were sorted by FACS. The HEK293-positive cells were pooled, expanded, and saved as polyclonal cell line. Alternatively, single HeLa-positive cells were sorted by sequential dilutions and one cell was expanded to establish monoclonal cell population (Fig. 1).

Preparation of viral samples

For NTA experiments, concentrated viral stocks were classically made by harvesting the culture medium after gently pipetting up and down (twice) on the adherent GFP-Gag producing cells to detach VLPs after 48 h of culture, and filtered through a 0.45 μm filter to remove cell debris or cells. VLPs were then concentrated by ultracentrifugation through a 20% sucrose cushion at 100,000 $\times$ g for 1.5 h at 4°C. The VLP pellet was resuspended with 100 μL of nanoparticle-free PBS, aliquoted and stored at $-$80°C.

Non-concentrated viral samples were also obtained to estimate viral production rate from a population of cells. To do this, 3 $\times$ 10^6 HeLa or 7 $\times$ 10^6 HEK293 cells were seeded in a 10-cm plate in F12 medium (10 mL). After 5 h of growth, the fluorescent cell proportion (NP_cell) was determined from more than 30 bright-field and fluorescence microscopy images of the culture dish. VLP-containing medium was collected and filtered as described above. Then, the cells were detached, washed with F12, and centrifuged at 1500 rpm at room temperature before counting using a Malassez counting chamber.

NTA experiments

NTA was performed with a NanoSight LM-10 instrument (Malvern Instruments, Malvern, UK) equipped with a blue laser module (488 nm) for fluorescent VLPs and NTA 2.0 software (Malvern Instruments).

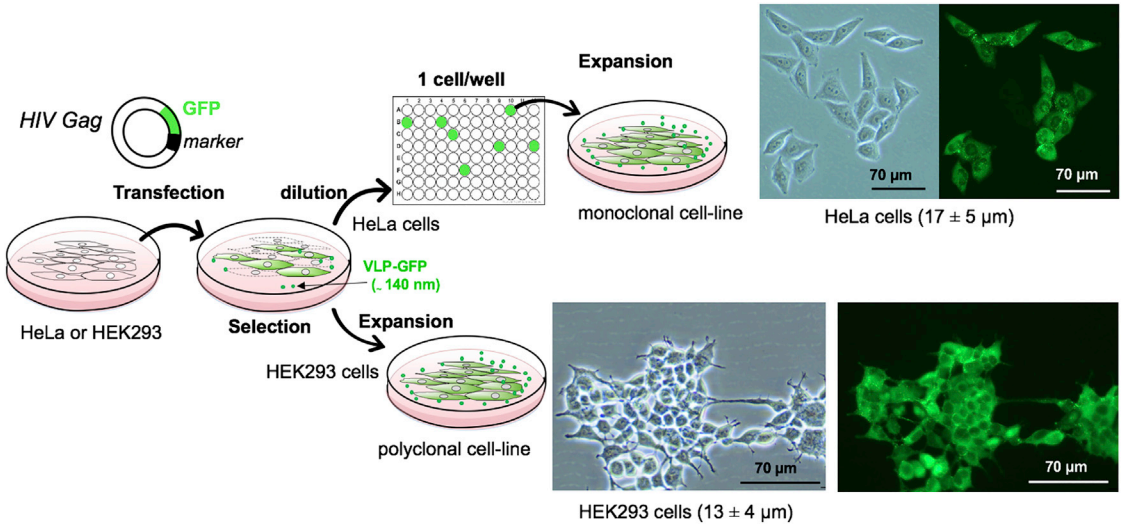

FIGURE 1 Cellular biology aspects of viro-fluidics. Schematic steps in the establishment of stable cell lines. Pictures are cells imaged after sorting with a 20× objective in bright field (left) and fluorescence (right). The cell culture showed ∼80% of fluorescent cells.

The camera was fixed at maximal level and flow rate was adjusted at 26 μL/min to have 10–100 particles/frame for reliable statistical analysis. Three movies of 60 s were captured at room temperature. Each movie was analyzed three times by using a set of optimized analysis parameters for detection of VLPs, which were kept constant during all measurements. The apparatus was calibrated using monodisperse fluorescent 100 nm beads (TetraSpek, 1.8 $\times$ 10^{13} particles/mL).

Design, fabrication, and operation of the microfluidic chips

The microfluidic devices were made from PDMS, which has several advantages, such as flexibility in device design, low cost, and proven properties for cell growth (33). Two different microarrays were designed with Clewin software:

1. The flow virometry chip (Fig. 2 *A*) has two identical parallel microchannels, 460 μm apart, 8 mm long, 130 μm wide. We used two different heights to test that all fluorescent VLPs were detected when transported at different speeds through the 40× objective field of view with heights of 3.7 or 6.7 μm. The projected half-height (h/2) of the channels was approximately 1.3- and 2.3 -fold of the depth of field (DOF = 1.44 μm) for h = 3.7 and 6.7 μm, respectively.
2. The viro-fluidic chip (Fig. 2 *B*) integrates single-cell capture and real-time detection of viruses produced. It has two inlets connecting a main channel (h = 18 μm and w_1 = 130 μm) that feed several parallel channels containing the single-cell trapping area. This area contains two pillars that capture the cell. These channels are followed by thinner channels (h = 4.3 μm) that define the virus detection area placed on a 40× objective (Fig. 2 *C*). To detect the produced VLPs passing in the flow, the sensing area is spaced 5 mm away from the cell traps to avoid bright cell fluorescence and photobleaching of intracellular GFP during VLP imaging (Fig. 2 *C*). Our field of view (40× objective, binning 2) limits the analysis to two whole sensing channels, simultaneously. The multiple trapping channels increased the probability of trapping two GFP cells contiguously, since cell samples also contained nonfluorescent cells (20%). Note that the hydrodynamic resistance in the virus detection zone decreases with the reciprocal number of channels.

Manufacturing protocol

The microfabrication was made in a clean room by standard photolithography using SU-8 photoresist. Layouts of the devices were transposed into a glass and chromium mask (Fig. 2, *A* and *B*) by the Laboratoire d'Analyse et d'Architecture des Systèmes (CNRS France). SU8 photoresist was spin coated on a 7.6-cm silicon wafer, exposed to UV, post baked, and developed. For the flow virometry chip, we planned the resist height at 4 $\pm$ 1 and 7 $\pm$ 1 μm, respectively. The heights of the reticulates were measured using a profilometer. These steps were repeated for each channel level. For the viro-fluidic device, an additional reactive ion etching procedure was made by applying a plasma etching process during 2 min (mixture CHF_3 and O_2 gazes) between the two photolithography steps. Thus, a small step of 100 nm deep was added in the silicon wafer to render the first SU8 layer visible during the alignment. Then, a standard PDMS replica molding process was used. A PDMS mix (Sylgard184) with a reticulating agent (10:1 PDMS/reticulate ratio) was prepared, degassed, poured onto the SU8/silicon master mold, and baked at 70°C for 2 h. PDMS chips were removed from the mold and sliced. Supply holes were punched, and chips were cleaned and permanently bonded on cleaned (acetone/isopropanol) coverslips using an O_2 plasma surface activation.

Operation

For flow virometry experiments, one microchannel was loaded with a viral sample and the other with a 100-nm fluorescent beads solution to focus at z = h/2. To characterize the flows inside the chip, the same beads were injected continuously into both channels using a microfluidic flow control system (Fluigent, Paris, France).

The viro-fluidics experiments were conducted as follows. After extemporaneous O_2 plasma treatment, the chip was washed for 1 h with F12 "conditioned" medium. This is an F12 medium supplemented with 10% fetal bovine serum and 1 μg/mL propidium iodide (PI) and diluted twice with a medium previously harvested from a dish of parental cells (nonproducing VLPs) grown to 40% confluence. PI is a dead cell stain that emits red fluorescence when bound to DNA. The serum prevented adherence of VLPs to PDMS and glass surfaces. Cell viability was monitored throughout the experiment by PI staining, a low cytotoxic dye. Then, the cells, freshly collected from a dish culture and adjusted at 10^5 cells/mL, were introduced in the cell perfusion well (I_2, Fig. 2 *B*), keeping the medium tap closed.

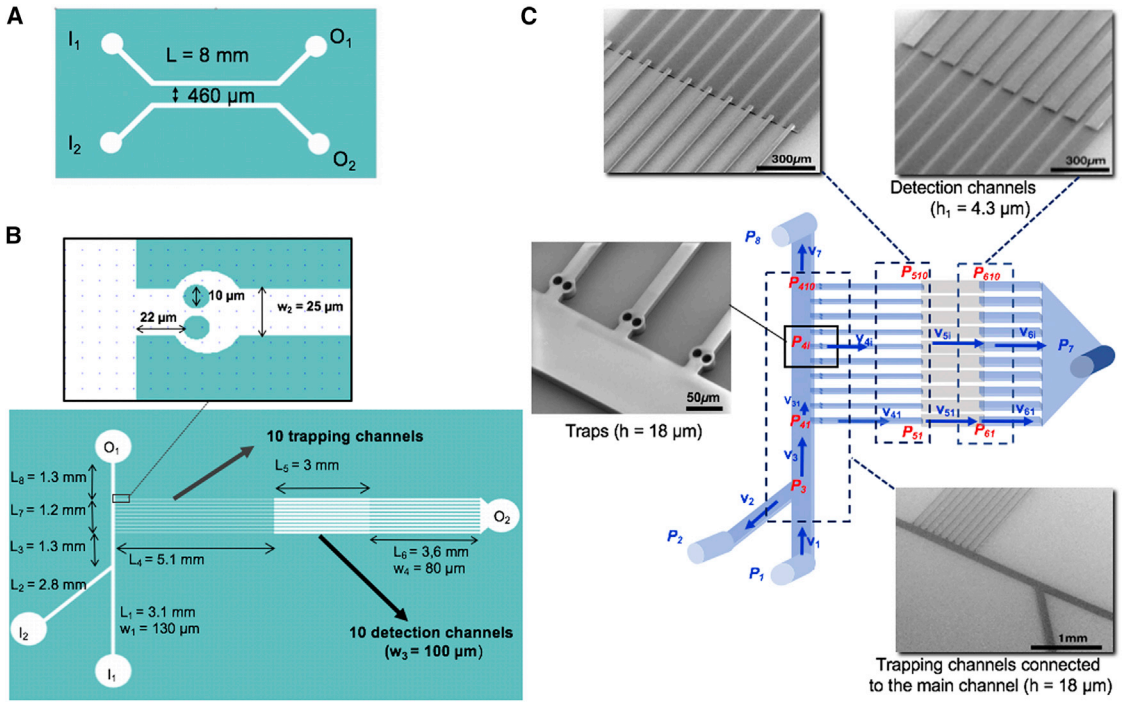

FIGURE 2 Microfluidic devices. (*A*) 2D-Clewin drawing of the virometry chip. The two identical microchannels have an inlet (I) and an outlet (O). (*B*) 2D-Clewin of the viro-fluidic chip. Ten individual trapping channels were disposed upstream of 10 detection channels and perpendicular to the main channel connecting the inlet (I_1) and outlet (O_1). Cells were perfused in I_2 and the viral particles exited through O_2. Lengths (Li) and widths (Wi) of each microchannel section are indicated. The upper inset gives an enlargement of a trap that was composed of two cylindrical pillars (d = 10 μm) separated by 4 μm. (*C*) Images of scanning electron microscopy of the master mold (gray rectangles) of the viro-fluidic chip show the photoresist (SU8) deposed on a Si wafer. The central drawing shows the trapping channels (h = 18 μm) in blue and the detection channels (h = 4.3 μm) in gray. The external applied pressures and average flow speeds in each channel section are shown in blue and the internal pressures in red.

When cells were trapped, the medium tap was opened and a pressure P_1 was applied in the inlet medium (I_1) to perfuse the captured cell with conditioned medium and to carry away the produced VLPs in the sensing channel, where they were monitored for several hours. This also caused a reflux toward the cell seeding well, flushing out extra cells and extra viral particles. A continuous flow toward the outlet well, O_1, was also insured. Throughout the experiment, the VLPs were imaged with a 40× objective placed under the virus detection area. However, brief interruptions were made to check cell viability by moving the objective lens to the trapping area and by decreasing the exposure time and the LED power.

Extended hydrodynamic model for the design of the viro-fluidic chip

For all experiments, the Reynolds number was lower than 0.02, much lower than 1 (microchannels height $<$ 18 μm and speeds less than a few mm/s). In this case the inertial term was neglected and, therefore, the Navier-Stokes equation reduces to the Stokes equation, and the flow was laminar. For a pressure-driven flow and a noncompressible Newtonian fluid, considering the following set of assumptions, the channel cross section was rectangular, the flow was steady and symmetric, the mass conservation was respected, the velocity was independent of x, and only the x component of the velocity was non-zero, Stokes equation could be reduced to:

$$\frac{\partial^2 v(y,z)}{\partial y^2} + \frac{\partial^2 v(y,z)}{\partial z^2} = -\frac{\Delta P}{\mu L}, \quad (1)$$

where ΔP was the pressure drop along the length L, and μ was the dynamic viscosity of the liquid.

Considering no-slip conditions on both walls (v(0) = v(h) = 0) and the geometrical parameters shown in Fig. 1 *S* (*left panel*), one gets the input flow rate Q and the average flow velocity v in a channel with a rectangular cross section (see (34) for a complete demonstration):

$$Q = \frac{\Delta P h^3 w}{12\mu L}\delta = \frac{\Delta P}{R_h} \quad (2)$$

$$v = \frac{Q}{S} = \frac{\Delta P}{R_h w h}, \quad (3)$$

where $\delta = 1 - \sum_{n,odd}^{\infty} \frac{1}{n^5}\frac{195}{\pi^5}\frac{h}{w}\tanh\left(n\pi\frac{w}{2h}\right)$ and $R_h = \frac{12\mu L}{h^3 w \delta}$.

δ depends only on the aspect ratio of the channel and tends to 1 for very wide channel in which the velocity profile is parabolic. For example, it is equal to 0.99 for the channels of 3.7 μm height and 130 μm width in the virometry chip. R_h is the hydrodynamic resistance of the channel.

In the case of a bifurcation (see, for example, Fig. S1, *right*), mass conservation of incompressible flow implies:

$$Q_m = Q_{s1} + Q_{s2} \Leftrightarrow v_m S_m = v_{s1} S_{s1} + v_{s2} S_{s2}, \quad (4)$$

where index m refers to the main channel and indexes s1 and s2 refer to the secondary channels.

When there is no bifurcation but only a cross section change, Eq. 4 simplifies in:

$$v_u S_u = v_d S_d. \quad (5)$$

Eqs. 4 or 5, combined with Eq. 3, can be applied to each linear section of the microfluidic circuit from the viro-fluidic chip and give a linear system. This system can be solved as it is or by analogy between hydrodynamic and electrical resistances (35) to calculate all the velocities as a function of initial known parameters (P1, P2, P7, P8, and the geometrical parameters depicted in Fig. 2, *B* and *C*). This simple model, without considering the trap hydrodynamic resistance, was used to predict the average velocities in the detection channels and set the operating pressure.

In the following, we use index i for the segment of length Li with respect to the notations shown in Fig. 2, *B* and *C*. Also, δ was calculated for each linear section: $\delta = 0.95$ (in the main channel), $\delta 1 = 0.56$ (trapping section), $\delta 2 = 0.97$ (detection), and $\delta 4 = 0.85$ (VLPs output section).

For the sake of simplicity, first we have considered the 10 detection channels as one, with the equivalent hydrodynamic resistance $R_{hdetection}$ of 10 identical parallel channels:

$$\frac{1}{R_{h,detection}} = \frac{10}{R_5 + R_6 + R_7}. \quad (6)$$

Thus, the problem is determining all the pressures. Eq. 4 expressed for bifurcations gives:

$$Q_1 = Q_2 + Q_3 \Rightarrow \frac{P_1 - P_3}{R_{h1}} = \frac{P_3 - P_2}{R_{h2}} + \frac{P_3 - P_4}{R_{h3}} \quad (7)$$

$$Q_3 = Q_{detection} + Q_8 \Rightarrow \frac{P_3 - P_4}{R_{h3}} = \frac{P_4 - P_7}{R_{h,detection}} + \frac{P_4 - P_8}{R_{h8}}. \quad (8)$$

This system of two equations (Eqs. 7 and 8) is solved straightforwardly because there are only two unknowns, P_3 and P_4. Then, considering that all pressure drops are the same in the 10 detection channels and equal to P_4-P_7, all internal pressure and average velocities can be solved. A numerical example is given in the Results and discussion.

To visualize the stream lines and validate calculus, the hydrodynamic model, including the pillar and cell presence, was completed by finite element computational fluid dynamic simulation (Comsol). Flow stream line speeds, shear rate (γ), shear stress on the cell membrane, and hydrodynamic resistances in trapping channels were computed.

Microscopy and image processing

We used a Nikon Ti2 inverted microscope equipped with a sCMOS back-illuminated camera Prime95B Photometrics (1200 × 1200 pixels and physical size of camera pixel of 11 μm). Illumination sources and emission filters for DAPI, GFP, and Cherry, were piloted by Nikon imaging software. Analyses were conducted with the dry objectives 10X Plan Apochromat (numerical aperture [NA] = 0.45), 20X and 40X Plan Apochromat (NA = 0.75). The microscope was placed in a chamber at 37°C under 5% CO_2. The moving particles were detected in the detection channels of the two chip types with the 40× objective with exposure time of 150 ms, binning 2, and 500 mW of LED power. The focus was done on the area at z = ∼ h/2. The field of view of the imaging system limits the analysis to two microfluidic detection channels simultaneously. The image pixel size was 11 μm*2/40, resulting in pixel width of 0.55 μm. In the case of 40× (NA = 0.75) and $\lambda_{emission}$ = 520 nm, the DOF was 1.44 μm.

All images and movies were treated with the Fiji software. Viral particles (or beads) were counted manually from videos by frame-by-frame analysis. Instantaneous speeds were calculated by dividing the distance (μm) that a nanoparticle ran during a frame by its duration (Fig. S2). The focus was made approximatively at half of the channel height, z = h/2, with the help of adhering beads in the reference channel. The maximum instantaneous speed (v_max) of a nanoparticle was calculated corresponding to the maximal flow line speed at z = h/2 and at y = w/2. Indeed, the integration of the streamlines velocities on the 100-nm bead surface provided an error less than 0.03% with respect to the central flow streamline speed when h = 3.7 μm and v = 400 μm/s. At least 30 nanoparticles were analyzed and we calculated thousands of instantaneous speeds from different VLP smears in the same 1-min video. To obtain the maximum flow speed, we retained the longest smear (i.e., z = h/2) that changes the least between two consecutive frames, meaning that the flowing particle diffused stochastically more in the *x* and/or *y* axis than in the *z* axis. When V_max was measured, the one-frame diffusion along the *x* axis was neglected when average flow speeds were higher than 75 μm/s, which represents 10 times more than 1D characteristic length of diffusion for a 100-nm bead (∼1.13 μm during 150 ms frame time). The hydrodynamic interparticle interactions were also neglected when particle concentration was lower than 10^6 particles/mL (36). Moreover, because δ is close to 1 in the virometry channels, the velocity profile can be considered as parabolic and the average flow velocity was calculated as v = 2/3 v_max.

The concentration of VLPs (C) was then calculated by dividing the number of particles (Np) counted during the time analysis interval (Δt) by the analyzed solution volume (Q* Δt):

$$C(particle/mL) = \frac{Np}{v * h * w * \Delta t}. \quad (9)$$

Knowing C and in consequence the total number of VLPs (Nt_VLPs = 10*C) produced by the productive cells (NP_cells, see Preparation of viral samples) during 5 h in 10 mL we found the average viral production corresponding to one single cell (Average_VLPs/h/cell):

$$\text{Viral production rate} = \frac{10 * C}{5 * NP\_cells} = \frac{2 * C}{NP\_cells} \quad (10)$$

RESULTS AND DISCUSSION

Flow virometry

The quantification of viral particles at low concentration in cell culture medium is not trivial (37–40). Nevertheless, we implemented a simple and sensitive microfluidic system for monitoring single viral particles produced at the single-cell scale (Fig. 3 *A*). The device must allow the detection of each VLP appearing in the analysis field.

To do so, a compromise had to be found between sensitivity of detection and flow speed. Two devices were fabricated with heights of 3.7 or 6.7 μm

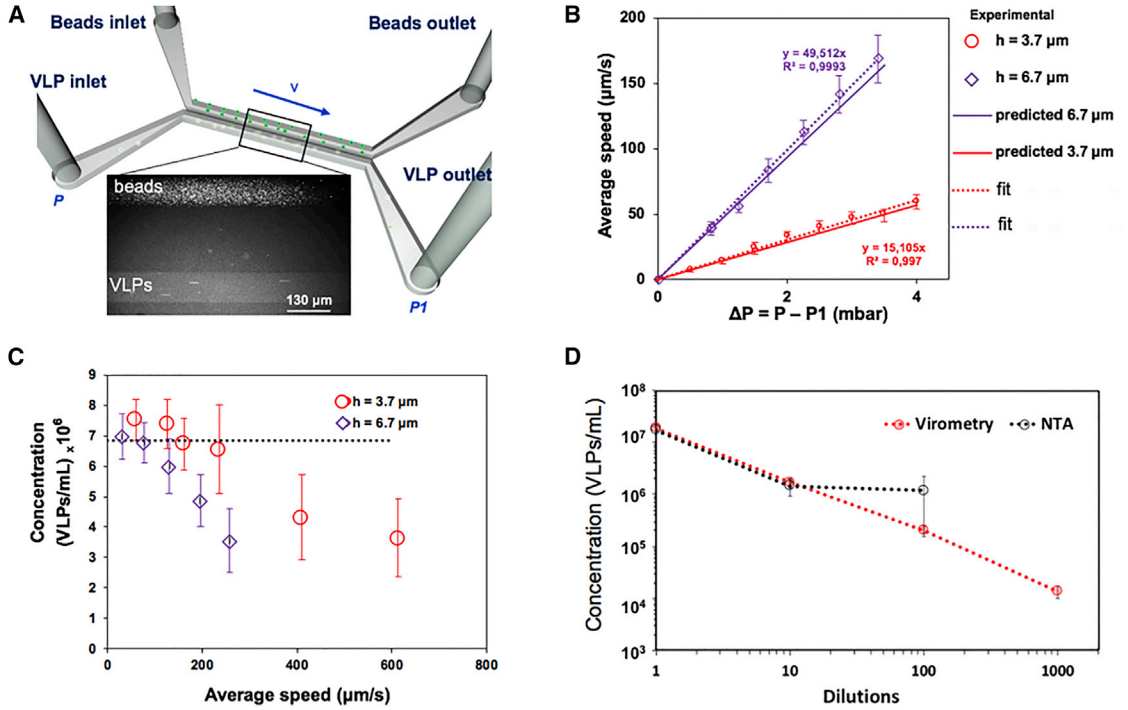

FIGURE 3 Flow virometry. (*A*) 3D representation of the detection chip showing the two parallel microchannels. One was filled with 100-nm fluorescent beads that adhered to the walls and served as reference for the second channel, which was used for imaging VLPs by fast optical video microscopy. The inset shows an image of the two channels obtained with a 20× objective. (*B*) Average speed (v) of beads as a function of the pressure between Inlet and Outlet ($P\text{-}P_1$); the 6.7- and 3.7-μm-high chips were tested. The dotted line represents the linear fit of the experimental mean speed and the solid lines the predicted v given by Eq. 3. (*C*). Concentration measurement for the same sample in F12 as a function of average flow speed (v), for both microchannel heights. The number of detected VLPs (signal/noise > 1.1) decreased for average speed of 300 and 130 μm/s for the 3.7- and 6.7-μm-high chips, respectively. The dotted line indicates the mean of the first 3 or 4 values of the measured concentrations. (*D*) Comparative analysis of the sensitivities of the flow virometry and NTA devices. The same PBS-diluted samples were analyzed by NTA or by the 6.7-μm-high detection chip. The NTA lost linearity for 1/100 dilution with no VLP detected for the 1/1000 dilution. In contrast, the flow virometry system remained reliable in the concentration range of 10^7 to 10^4 VLPs/mL. Experiments were performed in triplicate.

(as measured by a profilometer) and narrow width (130 μm), which harbored different hydrodynamic resistances. First, the flow speed was analyzed as a function of pressure drop ($P-P_1$) by perfusing fluorescent beads (500 beads/μL) in the reference channel (Fig. 3 *B*). Previously, it was checked that $P = P_1 = 0$ mbar was the equilibrium state with no liquid transport, while only a homogenous Brownian motion of beads subsisted with no relative displacement of beads. Then, as expected, we observed that the experimental values of average speeds followed a linear dependence in pressure drop for both channel heights. The predicted values given by Eq. 3 were also plotted (Fig. 3 *B*). The experimental heights deduced from the two fitted slopes (h = 3.7 and 7.1 μm, respectively) were similar to the values of photoresist measured in the clean room (h = 3.7 and 6.7 μm, respectively). Since the hydrodynamic laws were respected in the chips, they were validated for flow virometry.

Then, the tests were conducted with a nonconcentrated viral sample ($6.8 \pm 0.9 \times 10^6$ particles/mL) harvested from HeLa cell producing GFP-VLPs in F12 medium. Unlike beads, the viral particles showed different fluorescence intensities (Video S1) likely due to the variable number (2000–4000) of Gag-GFP molecules per VLP (23). The motion blur generated by the flow speed could also alter the sharpness of signals. Samples were analyzed with the two chips with h = 3.7 and 6.7 μm (Fig. 3 *C*). The number of detected VLPs decreased when the average flow speed exceeded 300 or 130 μm/s for chips with h = 3.7 or 6.7 μm, respectively. Indeed, for high speeds and despite the diffusion of VLPs in the *z* axis, some of them stayed out of the DOF limits of the 40× objective before leaving the field of view. We concluded that the detection performance of both chips was equivalent at low flow speeds, and that the 3.7-μm high chip with an h/2 approximating 1.3*DOF had the advantage of remaining efficient over a wider speed range. For these two detection speed limits (300 and 130 μm/s), the flow rates were $Q_{3.7\mu m} = 130*3.7*300 = 1.44*10^5$ $\mu m^3/s$ and $Q_{6.7\mu m} = 130*6.7*130 = 1.13*10^5$ $\mu m^3/s$, respectively. This

showed that the sample processing time could be reduced by 1.3 times ($Q_{3.7\mu m}$/ $Q_{6.7\mu m}$) with the 3.7-μm high chip, but that the accuracy decreased as these speed limits were approached (Fig. 3 *C*).

The performance of our flow virometry system with a lower speed range detection performance ($h = 6.7\ \mu m$) was compared with that of the commercial NanoSight instrument, a gold standard for measuring nanoparticles concentration. The NTA performs reliable measurements for concentrations between 10^7 and 10^9 particles/mL within a nanoparticle detection range of 10 and 100 particles/frame. A recent study showed that the low limit of detection of this apparatus is 1.7×10^7 VLPs/mL (31). Therefore, we had to concentrate our samples by ultracentrifugation for the comparative study (see Materials and methods). The concentrations ($1.40 \pm 0.03 \times 10^8$ VLPs/mL) determined by NTA (Fig. S3 *A*) were close (with a deviation of 12.5%) to that determined by the 6.7-μm height chip ($1.6 \pm 0.2 \times 10^8$ VLPs/mL), revealing the reliability of our system. To determine the concentration range that maintains the linear regime of our detection system, a series of successive dilutions were performed in PBS, starting from a sample at 1.75×10^7 VLPs/mL (Dilution 1). VLP concentrations were measured either by NTA or by the 6.7-μm-high chip, when $v < 130\ \mu m/s$ (Fig. 3 *D*). Unlike NTA, our system remained reliable for concentration of 10^4 VLPs/mL (Video S2). Our system has the advantage of detecting fluorescent particles in the entire volume of the microchannel while the NTA uses a flow chamber ($h = 50\ \mu m$ and $w = 1$ mm) with dimensions much larger than the laser focusing beam (axial depth, 10 μm and lateral field view, 500 μm, 20× objective), requiring strong statistical analysis. For highly diluted solutions, the NTA signals were noisy, and unreliable peaks were obtained (Fig. S3 *B*).

In addition, the NTA allows simultaneous characterization of the nanoparticle sizes. Since aggregation of two viral particles is rarely encountered for concentrations $\leq 4 \times 10^7$ VLPs/mL (41), size analysis was conducted with a diluted viral sample ($1.14 \pm 0.13 \times 10^7$ particles/mL). We found 93% of particles with diameter $d = 148 \pm 16$ nm and 7% with $d = 315 \pm 26$ nm, which might correspond to 2-aggregated viral particles (Fig. S3 *C*). The size of our VLPs was similar to those determined by chromatography (174 ± 60 nm) (31) or cryoEM (140 ± 20 nm) (42) and also to the measured sizes of complete HIV-1 (119–207 nm) (41,43,44). Furthermore, an advanced optical trapping approach for fluorescent HIV-1 using optical tweezers showed that aggregation of two viruses rarely occurred for concentrations $\leq 4 \times 10^7$ VLPs/mL, suggesting a low probability of aggregation when studying virus production of single cells.

A viro-fluidic system for real-time analysis of virus production kinetics from a single cell

The sensitivity of our virometry system allowed us to measure viral particle production at the single-cell scale. To record and quantify live virus egress from a single cell, a chip that combines cell capture and virus detection was needed. There is an extensive literature on single-cell trapping, mainly for intracellular analyses, demonstrating that a PDMS device is a suitable system for cell culture and that immobilization does not alter cell properties (1,2,14,20,45–48). To analyze the VLP produced from each individual cell, we took advantage of the flow to separate and move the newly formed fluorescent VLPs away from the fluorescent-producing cells. To this end, the cell trap channel was directly connected to the virus detection channel. Here we implemented the detection system with $h = \sim 4.3\ \mu m$ to benefit from a sensitive detection in a wide range of flow speeds. Since the field of view of our imaging system allowed two detection channels to be viewed simultaneously, we designed a chip with several parallel channels (Fig. 2, *B* and *C*). Channel multiplication (10 cell trapping channels individually connected to 10 virus detection channels) increases the probability of trapping two productive cells (green and alive) contiguously since the cell samples perfused into the chip contained nonfluorescent cells (~20%) and also reduces the hydrodynamic resistance in the sensing area. Although, after a few hours of analysis, the study of additional cells could be undertaken by shifting the microscope stage to other channels, in general we analyzed two cells per cell sample per day. Throughout the experiment, the cells were perfused with a conditioned medium that mimics the environment of the cell population. It contains metabolites, growth factors, and extracellular matrix proteins secreted by the cell population. A fluorescent marker (PI) was also added to the medium to monitor cell viability.

As with the virometry chip and based on the system of Eqs. 7 and 8 ($\delta 1 = 0.56$), the external pressure was optimized so that the average speed of the released particles did not exceed the detection threshold of 300 μm/s and to avoid cross-contamination by the cells at the inlet I_2. Fig. 4 *A* shows two HeLa cells immobilized for several hours in adjacent channels. The pressures P_1, P_2, P_7, and P_8 (Fig. 2 *C*) were fixed to 7.9, 5.5, 0, and 5.5 mbar, respectively, when $v_{5i} = 250 \pm 18\ \mu m/s$ (Video S3). Next, application of the law of flow rate conservation allowed us to estimate the average speed in the trapping channel, $v_{4i} = 239 \pm 17\ \mu m/s$. Importantly, all VLPs produced by a trapped cell were transported to their respective detection channel. Experimentally, inspection of the channel with empty trap adjacent to that of Cell1 revealed the

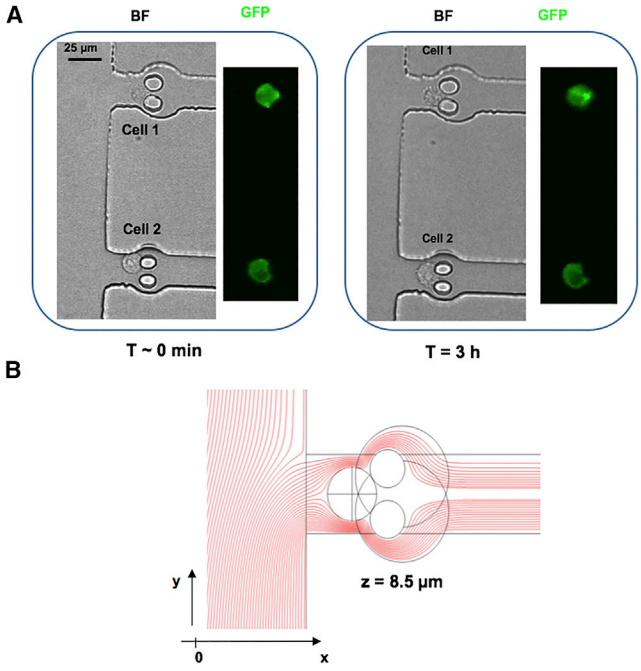

FIGURE 4 Single cell trapping in the viro-fluidic chip. (*A*) Representative image of two productive green single cells captured in two adjacent channels. Cells were imaged in BF and GFP (40× objective) at 1 min before looking at the detection channel and starting the recording session ($T_0 = 0$ min) and after 3 h of video recording. (*B*) Comsol simulation of streamlines at $z = 8.5$ μm in the vicinity of a 17-μm trapped bead when the average flow speed in the trapping channel (v_{4i}) was 239 μm/s. No local looping of streamlines was observed, ensuring the absence of contamination between the 10 parallel trapping channels.

absence of VLP contamination that could originate from Cell2 or the I_2 inlet (cells perfusion) (Fig. 2 *B*). This was also ensured by the regularity of the flow near the trapped cell. The evolution of streamlines in the vicinity of a trapped 17-μm bead was simulated with Comsol and no local recirculation flow appeared when $v_{4i} = 239$ μm/s. One example for one XY section plane at $z = 8.5$ μm is given in Fig. 4 *B*. The streamline speeds around a trapped cell and the shear stress are displayed in Fig. S4, *A* and *B*. The simulation showed a maximal shear rate of 1000 s^{-1}, which corresponded to a shear stress (τ) = 1 Pa (Fig. S4 *A*). This value is close to physiological conditions since circulatory lymphocytes or endothelial cells in blood capillaries undergo a maximal shear stress of 1.33 and 0.72 Pa, respectively (49). In addition, the trapped cells remained intact after 3 h of immobilization (Fig. 4 *A*). Cell viability was also monitored at different pressures using PI staining. As shown in Fig. S5, cells were dying when $P_1 > 25.5$ mbar and $\tau > 3.8$ Pa. Extensive Comsol simulations allowed 3D views of the shear rates around 17- and 10-μm beads that mimicked HeLa nucleus when a cell was fully spread (50) (Fig. S6 *A*). Simulations also allowed the evaluation of the additional hydrodynamic resistance in the trapping channel due to the presence of the pillars with or without cells (Fig. S6 *B*). By adding in the system of Eqs. 7 and 8, the value corresponding to an adherent cell ($\delta 1' = 0.28$), we predicted $v_{4i} = 206$ μm/s and $v_{5i} = 217$ μm/s.

Once a single cell was trapped, real-time analysis of released VLPs began at the sensing channel. The fluorescent particles were monitored for at least 1 h, and 3-min movies were analyzed frame by frame (Video S3). First, viral production of 15 single HeLa cells from $\geq$10 cell samples taken on different days from the same monoclonal line (Fig. 1) were analyzed to assess the reproducibility of the system. As an example, the production at a given time of Cell1 and Cell2 of Fig. 4 *A* are shown in Fig. 5 *A*, and a representative kinetic plot with the number of VLPs detected every 30 s (arbitrary step) is shown in Fig. 5 *B* (*black dots*). The interruptions in the recording of Cell1 or Cell2 production were due to several inspections of the trapped cell and the different channels of the chip. During the 4 h of recording, there was no reflux, no interchannel contamination of VLPs, and no VLP adhesion to surfaces, whereas 207 VLPs were detected in the two sensing channels of Cell1 and Cell2, corresponding to a VLP concentration of $\sim 1.8 \times 10^5$ VLPs/mL. In general, for all cells the production rate decreased over time. For example, for Cell1 the production rates were 85, 73, and 41 VLPs/h after 1, 2, and 3 h of analysis. For all HeLa cells, an average production rate of 41 $\pm$ 4 VLPs/h/cell was determined (Fig. 5 *C*). The variation between measurements (11%) should correspond to the cell heterogeneity. A bootstrap analysis of the data indicates that analysis of 15 cells was statistically sufficient. In parallel, a global estimation of the viral production of a population of the same cells was performed. The VLP-containing medium of a plate of monoclonal HeLa cells, cultured for 5 h, was analyzed using the virometry chip and/or by NTA and the producing cells were trypsinized and counted (see Materials and methods). The viral production per hour and by cell calculated from this cell population gave an average rate of 53 $\pm$ 8 VLPs/h/cell (Fig. 5 *D*), which was comparable with that obtained with individual cells. Overall, these results indicate that trapping and flow did not interfere with the viral production of the cell, that the viro-fluidics measurements were not affected by contaminating cells or VLPs, and that all viral particles released from the trapped cell were carried and detected efficiently in the detection channel. These data demonstrate the reliability of our viro-fluidic system.

Viro-fluidics was also used to study the viral production rate and kinetics of VLP release from the human HEK293 cell line, another model classically used to study HIV biogenesis. This time, a polyclonal cell line was used

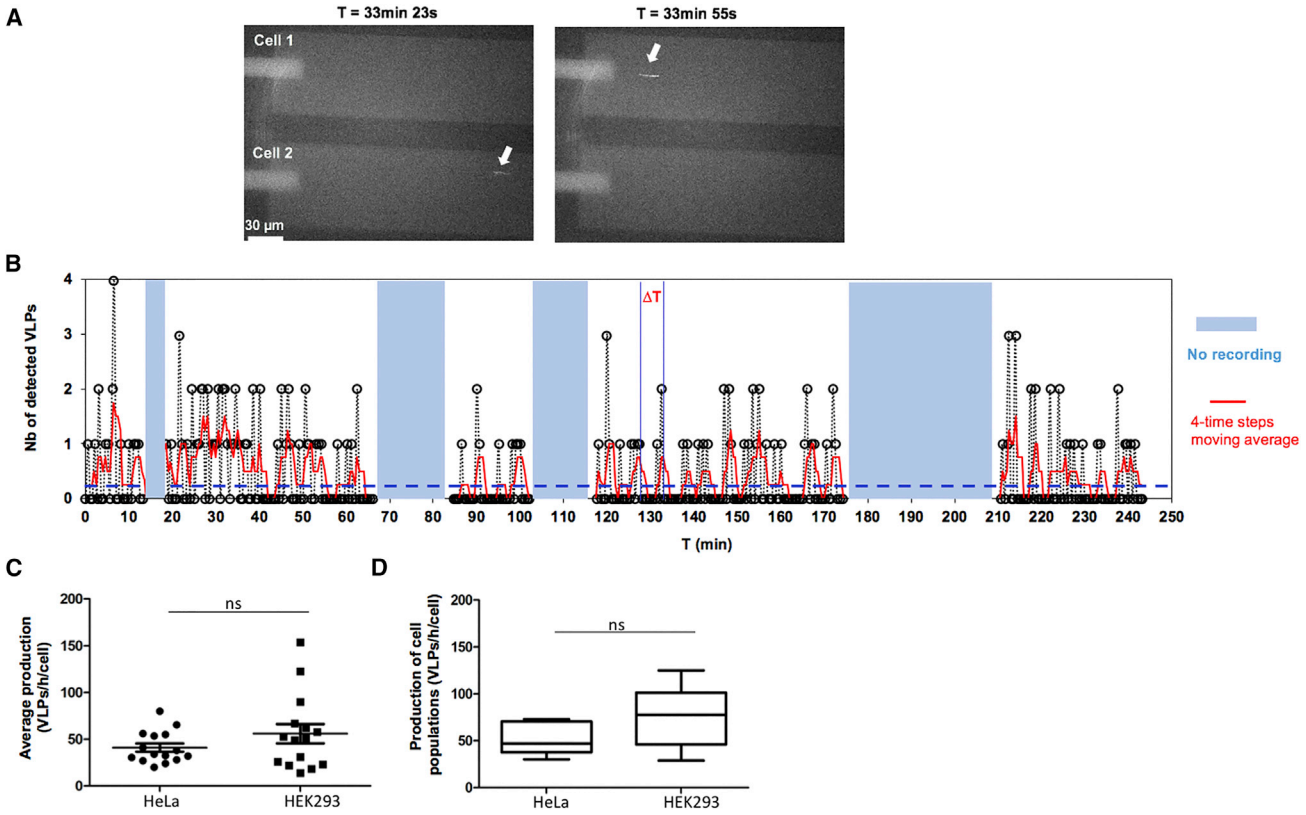

FIGURE 5 Live detection of viral production of single cells. (*A*) Images showing the passage through the detection channel ($w_3 = 100\ \mu m$) of VLPs released from the two cells of Fig. 4 *A*. The pressures P_1, P_2, P_7, and P_8 (Fig. 2 *C*) were set at 7.9, 5.5, 0, and 5.5 mbar, respectively. The average speed of VLPs in the detection channel was $v_{5i} = 250\ \mu m/s$. (*B*) Number of VLPs (*black dots*) detected every 30 s for the Cell1 in Fig. 4 *A*. T_0 is the start of the recording. The dotted blue line indicates the threshold set at 0.25, due to the four-step moving average (1/4). The red line represents the moving average for continuous times of four steps and ΔT the representative time interval between two peaks, also noted in red. The nonrecording intervals (in *blue*) correspond to the inspection of captured cells to check their viability or of other channels to ensure the absence of reflux or virus contamination. (*C*) Average productions of VLP_S released from individual cells ($n = 15$). Groups were compared using Student's *t*-test; ns, not significant ($p = 0.19$). (*D*) VLP productions determined from respective cell populations grown in tissue-culture dishes ($n = 5$, $p = 0.19$).

(Fig. 1) to get a broader view of the cell-to-cell variation of viral production. As above, the viral production of 15 individual cells were studied and an average rate of production was determined (56 ± 10 VLPs/h/cell) (Fig. 5 *C*). The kinetics were similar to those obtained with HeLa cells with greater intercellular variation in production rate (18%) as expected for a polyclonal cell line. For comparison, an overall estimate from the polyclonal HEK293 population, cultured for 5 h in a culture dish, gave an average rate of 78 ± 16 VLPs/h/cell (Fig. 5 *D*). This value was similar to that obtained for the average of the individual cells (Fig. 5 *C*). This rate was threefold higher than the VLP productivity determined by NTA by González-Domínguez et al. with HEK293 cells transiently expressing HIV-1 Gag-GFP during 72 h (30). The difference between the expression systems used could explain this discrepancy. In the end, both cell types, HeLa and HEK293, showed similar viral production kinetics, suggesting the use of similar mechanisms of biogenesis and release of viral particles.

Interestingly, the kinetic profiles of the single-cell production appear nonregular with alternating nonproduction, low and high ("bursts") production of VLPs (*black dots* in Fig. 5 *B*). A simple way to gather the detected VLPs under one curve (*red curve* in Fig. 5 *B*) was to apply a four-point moving average analysis (a compromise between two-point (1 min), which is the minimal moving interval, and a six-point (3 min) moving average (Fig. S7)). Times between 2 consecutive bursts (ΔT) were identified for 15 cells of each cell type (∼450 ΔT identified for each cell type). For all cells, ΔT had a normal distribution with ΔT averages (<ΔT>) fluctuating around 3.8–4 min for HeLa and HEK293 cells, respectively, and the bursts arrived randomly in the detection zone. Note that the ΔT values were shorter with larger amplitudes during the first hour of cell residence in the chip, signifying a higher production rate, as shown by the red line for Cell1 in Fig. 5 *B*. These initial bursts correspond to the time of cell adhesion as seen under the microscope. The curvature of the membrane

of nonadherent cells reduces the energy barrier for Gag assembly, thus facilitating virus egress (51,52). Also, Gag synthesis might be stimulated in cells freshly detached by the trypsin from the culture dish (53). As the viral production rate (VLPs/h) decreased with time, the $<\Delta T>$ values were calculated from the ΔT determined for the same intervals of 1 h. But when the change in the production rate was rapid, we averaged the ΔT over 30-min intervals (in order not to average out productions that are too different) (Fig. 6). This explains why the number of data points in the graph exceeds the number of analyzed cells. For the entire range of 34.5–232 VLPs/h, the $<\Delta T>$ fluctuated around 3.5 ± 1.3 min and a linear tendency with high variability can be inferred for both cell lines (Fig. 6). To test whether this behavior is specific to cell production, control experiments were conducted with diluted VLP samples that were not produced by the trapped cells (Fig. S8 *A*). For this purpose, viral stocks, at different concentrations ($2–20 \times 10^5$ VLPs/mL), were directly injected into the chip in the absence of producer cells in the traps. Then, VLP detection was conducted by using the same experimental conditions and pressures as for the producer cells to compare experiments with the same rates (VLPs/h). On first inspection of Fig. S8 *A*, the kinetics profile of the control (*black dots*) was similar to that of the productive cells. The four-point moving average (MATLAB, The MathWorks, Natick, MA) also showed a nonmonotonic profile. However, some visual differences between the kinetics of productive cells and controls could be noticed: when VLPs/h < 45, the peaks of

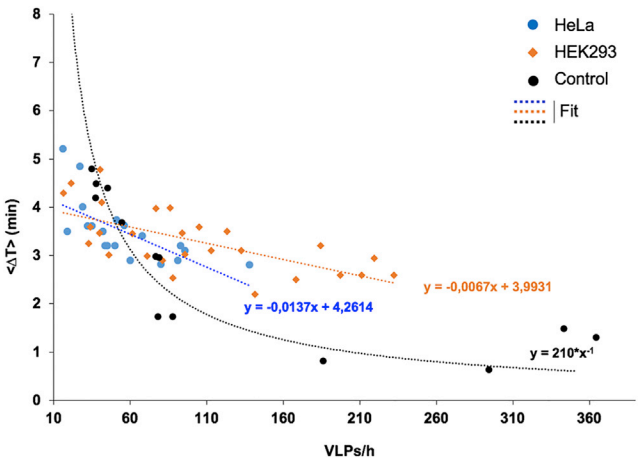

FIGURE 6 Analysis of viral production timescales. Average of ΔT ($<\Delta T>$) was calculated from ΔT defined from four-point moving average (*red curve* in Figs. 5 *B* and S8 *A*) and was plotted as a function of the number of detected VLPs per hour. The control experiment consisted of injecting VLP samples directly into the chip (*black dots*). The black dotted line corresponds to power law fit $y = a*x^b$, with $a = 210$ and $b = -1$ and differs from that of the single VLP-producing cells (*red* and *blue fitting lines*).

the green cells were more numerous and contained less VLPs than the controls and, conversely, when VLPs/h > 90 (see, for example, *red curves* in Fig. 5 *B* for the interval 87–172 min and the control in Fig. S8 *A*). For 13 controls, $<\Delta T>$ was also plotted in functions of number of detected VLPs/h (Fig. 6). The control data showed a different behavior with respect to producing cells. This behavior could be qualitatively explained by relating the average $\Delta T \sim 1/(cQ)$ (which was derived from Eq. 9 with $Np = 1$) to the number of detected VLPs/h given by 1 h/ΔT. These results showed a qualitative and quantitative difference between the viral release from the cells and the control system in which ΔT values were solely driven by flow properties and not by a biological process. This difference was also observed when evaluating the frequency of VLP bursts by a fast Fourier transform using a MATLAB program (Figs. S8 *B* and S9 *B*). These fast Fourier transform analyses revealed typical frequencies ($1/<\Delta T>$) for the productive cells and the absence of a characteristic frequency for the control. The existence of a typical time for green cells suggests the presence of limiting step(s) in the virus formation mechanism. With the producing cells, the frequency increased with the production rate (0.0038–0.0025), as shown in the profile of the $<\Delta T>$ plotted against VPLs/h in Fig 6. The fits for cell productions were linear with no zero slope, meaning that the cells could not maintain the same frequency as VLPs/h varied (Fig. 6). Although the ΔT values were normally distributed and stochastic (see probability density function in Fig S7), the frequency ($1/ < \Delta T>$) increased when a cell had to produce more VLPs per unit time, suggesting a limitation of VLP production in a short time. The solution would be for the cells to increase the burst frequency to have fewer VLPs per burst. At this time, we are not able to propose a simple model or biological explanation for these results. Perhaps there is a Gag supply limitation process that imposes an upper limit on VLP formation. In the literature, HIV transcriptional bursting has been reported that is due to stochastic transcriptional pausing (54,55). Among the different durations reported, some might lead to similar delays. Our data could also reflect the supply of Gag proteins for virus assembly and release that also takes minutes (29). Further extensive research is needed to understand the mechanism(s) responsible for these stochastic bursts whose typical onset time apparition is on the order of 3.5 ± 1.3 min.

One might envision that the optimal strategy for a virus is to reproduce as quickly as possible with a production that increases gradually over time. However, maximal rate might not be the optimal strategy when the immune response may kill the cell. Mathematicians are developing theoretical models of the dynamics of

HIV infection. They suggested two stochastic models of viral production from infected cells (56,57): the "continuous" production model in which once a cell is infected it produces virus continuously throughout its life, and the burst model in which the infected cell produces intracellular viruses until a critical number is reached and releases all its viruses in a single burst simultaneous with its death. These models include many parameters (infection during lifespan scale time of days and cell-virus clearances). Our experimental model does not fit to the burst model since viral particles do not accumulate inside HeLa or HEK293 cells before their release. Our experimental data suggest that each cell stochastically produces viruses at similar mean rate ($\sim$50 VLPs/h). Assuming that rate remains constant during all cell life, then our data should support the continuous model. As discussed in (56), HIV production could vary by cell type, depending on its lifespan. Massive and rapid viral production (burst model) could be achieved by cells with a short lifespan (days), while moderate and slow viral production (continuous model) could be achieved by infected macrophages with a longer lifespan (weeks). However, macrophages (and not lymphocytes) harbor intracellular compartments where HIV particles assemble and accumulate, and therefore seem to be more suitable for viral release in burst. Further viro-fluidics studies about viral production (burst size and dynamics) at the individual cell level should bring some light to test the assumptions and predictions of these different mathematical models. This study highlights the importance of single-cell virology in improving the understanding of the molecular and cellular basis of virus-host interactions.

CONCLUSIONS

Here, we developed a simple and sensitive technique employing hydrodynamic cell trapping in a narrow individual microchannel allowing the live quantification of viral release in the extracellular medium at the single-cell and single-particle scales. This study revealed the rate, frequency, and kinetics of HIV-1 VLP release from a single cell and uncovered a typical signature of release kinetics that would have been masked in population-scale experiments or in an uncoupled strategy in which viruses must be harvested at long time intervals (30 min) (58).

It would have been interesting to compare these new data with the literature on HIV infection in patients. Unfortunately, limited and conflicting quantitative studies in vivo have estimated that one infected T-cell produces between 500 and 4000 viruses during its lifetime (59,60). To our knowledge, there are no more precise experimental data available in the literature.

Viro-fluidics will open new avenues in our understanding of the dynamics of virus egress and will allow the analysis of the cellular and viral factors involved. In the future, several cell lines will be studied providing new information on the adaptive strategies of HIV-1 production to its host. To date, these data are missing because they are inaccessible by conventional approaches.

The applications of viro-fluidics are numerous. Indeed, viro-fluidics is not only dedicated to HIV but also allows the study of different viral diseases, such as other pandemic viruses. Since it is applicable to body fluids, it allows for the first time to study the biogenesis, the release pathway, and the propagation of these pathogens within the host environment.

SUPPORTING MATERIAL

Supporting material can be found online at https://doi.org/10.1016/j.bpr.2022.100068.

AUTHOR CONTRIBUTIONS

M.M. conceptualized the study, analyzed and interpreted the data, and wrote the manuscript with the help of M.S. J.E. and M.S. conducted the experiment with technical help of J.F., and analyzed and interpreted the data. B.C. and M.S. designed the chips and B.C., M.S., and J.E. fabricated the devices. A.N. performed the simulations. E.M. and L.C. contributed to the microscopy, the video analysis, and the mathematical analysis and data interpretation. All authors supervised and revised the manuscript.

ACKNOWLEDGMENTS

We are grateful to the Montpellier MRI imaging staff for technical assistance for microscopy and FACS. We thank the staff of the IES clean room for their assistance with special thanks to Dr. F. Pichot. Many thanks to Dr. J. Chopineau and Dr. M. Morille for their expertise in NTA experiments, and to C. Motto-Ros, trainee, for technical help. J.E. is supported by a fellowship from Infectiopole Sud. This study was supported by grants of the French National Agency for Research on AIDS and viral hepatitis (ANRS) to M.M., B.C., and E.M., the CNRS-Osez L'Interdiciplinarité to M.M., and the French National Research Agency (ANRJC) to M.S. MRI and the CBS belong to the France-BioImaging national infrastructure supported by the French National Research Agency (ANR-10-INBS-04, "Investments for the future").

DECLARATION OF INTERESTS

The authors declare no competing interests.

REFERENCES

1. Huang, N.-T., H.-I. Zhang, …, K. Kurabayashi. 2014. Recent advancements in optofluidics-based single-cell analysis: optical on-chip cellular manipulation, treatment, and property detection. *Lab Chip.* 14:1230–1245. https://doi.org/10.1039/C3LC51211H.
2. Narayanamurthy, V., S. Nagarajan, …, T. M. Sridhar. 2017. Microfluidic hydrodynamic trapping for single cell analysis: mechanisms,

methods and applications. *Anal. Methods.* 9:3751–3772. https://doi.org/10.1039/C7AY00656J.

3. Mazutis, L., J. Gilbert, …, J. A. Heyman. 2013. Single-cell analysis and sorting using droplet-based microfluidics. *Nat. Protoc.* 8:870–891. https://doi.org/10.1038/nprot.2013.046.
4. Ciuffi, A., S. Rato, and A. Telenti. 2016. Single-Cell Genomics for Virology. *Viruses.* 8:E123. https://doi.org/10.3390/v8050123.
5. Liu, W., H. He, and S. Y. Zheng. 2020. Microfluidics in Single-Cell Virology: Technologies and Applications. *Trends Biotechnol.* 38:1360–1372. https://doi.org/10.1016/j.tibtech.2020.04.010.
6. Chaipan, C., A. Pryszlak, …, C. A. Merten. 2017. Single-Virus Droplet Microfluidics for High-Throughput Screening of Neutralizing Epitopes on HIV Particles. *Cell Chem. Biol.* 24:751–757.e3. https://doi.org/10.1016/j.chembiol.2017.05.009.
7. Jaitin, D. A., E. Kenigsberg, …, I. Amit. 2014. Massively parallel single-cell RNA-seq for marker-free decomposition of tissues into cell types. *Science.* 343:776–779. https://doi.org/10.1126/science.1247651.
8. Prakadan, S. M., A. K. Shalek, and D. A. Weitz. 2017. Scaling by shrinking: empowering single-cell 'omics' with microfluidic devices. *Nat. Rev. Genet.* 18:345–361. https://doi.org/10.1038/nrg.2017.15.
9. Streets, A. M., X. Zhang, …, Y. Huang. 2014. Microfluidic single-cell whole-transcriptome sequencing. *Proc. Natl. Acad. Sci. USA.* 111:7048–7053. https://doi.org/10.1073/pnas.1402030111.
10. Guo, F., S. Li, …, C. E. Cameron. 2017. Single-Cell Virology: On-Chip Investigation of Viral Infection Dynamics. *Cell Rep.* 21:1692–1704. https://doi.org/10.1016/j.celrep.2017.10.051.
11. Akpinar, F., A. Timm, and J. Yin. 2016. High-Throughput Single-Cell Kinetics of Virus Infections in the Presence of Defective Interfering Particles. *J. Virol.* 90:1599–1612. https://doi.org/10.1128/JVI.02190-15.
12. Warrick, J. W., A. Timm, …, J. Yin. 2016. Tools for Single-Cell Kinetic Analysis of Virus-Host Interactions. *PLoS One.* 11:e0145081. https://doi.org/10.1371/journal.pone.0145081.
13. Shafiee, H., S. Wang, …, U. Demirci. 2015. Emerging technologies for point-of-care management of HIV infection. *Annu. Rev. Med.* 66:387–405. https://doi.org/10.1146/annurev-med-092112-143017.
14. Ramji, R., V. C. Wong, …, K. Miller-Jensen. 2015. A passive-flow microfluidic device for imaging latent HIV activation dynamics in single T cells. *Integr. Biol.* 7:998–1010. https://doi.org/10.1039/c5ib00094g.
15. Powell, L., R. S. Wiederkehr, …, W. O. Osburn. 2018. Rapid and sensitive detection of viral nucleic acids using silicon microchips. *Analyst.* 143:2596–2603. https://doi.org/10.1039/C8AN00552D.
16. Ouyang, W., and J. Han. 2019. Universal amplification-free molecular diagnostics by billion-fold hierarchical nanofluidic concentration. *Proc. Natl. Acad. Sci. USA.* 116:16240–16249. https://doi.org/10.1073/pnas.1904513116.
17. Yucha, R. W., K. S. Hobbs, …, T. J. Henrich. 2017. High-throughput Characterization of HIV-1 Reservoir Reactivation Using a Single-Cell-in-Droplet PCR Assay. *EBioMedicine.* 20:217–229. https://doi.org/10.1016/j.ebiom.2017.05.006.
18. Golumbeanu, M., S. Cristinelli, …, A. Ciuffi. 2018. Single-Cell RNA-Seq Reveals Transcriptional Heterogeneity in Latent and Reactivated HIV-Infected Cells. *Cell Rep.* 23:942–950. https://doi.org/10.1016/j.celrep.2018.03.102.
19. Rato, S., A. Rausell, …, A. Ciuffi. 2017. Single-cell analysis identifies cellular markers of the HIV permissive cell. *PLoS Pathog.* 13:e1006678. https://doi.org/10.1371/journal.ppat.1006678.
20. Eid, J., M. Mougel, and M. Socol. 2020. Advances in Continuous Microfluidics-Based Technologies for the Study of HIV Infection. *Viruses.* 12:982. https://doi.org/10.3390/v12090982.
21. Dirk, B. S., L. R. Van Nynatten, and J. D. Dikeakos. 2016. Where in the Cell Are You? Probing HIV-1 Host Interactions through Advanced Imaging Techniques. *Viruses.* 8:E288. https://doi.org/10.3390/v8100288.
22. Göttlinger, H. G. 2001. The HIV-1 assembly machine. *AIDS.* 15. S13-20.
23. Lavado-García, J., I. Jorge, …, L. Cervera. 2021. Characterization of HIV-1 virus-like particles and determination of Gag stoichiometry for different production platforms. *Biotechnol. Bioeng.* 118:2660–2675. https://doi.org/10.1002/bit.27786.
24. Tohidi, F., S. M. Sadat, …, R. Yaghobi. 2017. Construction and Production of HIV-VLP Harboring MPER-V3 for Potential Vaccine Study. *Curr. HIV Res.* 15:434–439. https://doi.org/10.2174/1570162X15666171017122229.
25. Chamontin, C., P. Rassam, …, M. Mougel. 2015. HIV-1 nucleocapsid and ESCRT-component Tsg101 interplay prevents HIV from turning into a DNA-containing virus. *Nucleic Acids Res.* 43:336–347. https://doi.org/10.1093/nar/gku1232.
26. Ferrer, M., C. Clerté, …, M. Mougel. 2016. Imaging HIV-1 RNA dimerization in cells by multicolor super-resolution and fluctuation microscopies. *Nucleic Acids Res.* 44:7922–7934. https://doi.org/10.1093/nar/gkw511.
27. Ivanchenko, S., W. J. Godinez, …, D. C. Lamb. 2009. Dynamics of HIV-1 Assembly and Release. *PLoS Pathog.* 5:e1000652. https://doi.org/10.1371/journal.ppat.1000652.
28. Jouvenet, N., P. D. Bieniasz, and S. M. Simon. 2008. Imaging the biogenesis of individual HIV-1 virions in live cells. *Nature.* 454:236–240. https://doi.org/10.1038/nature06998.
29. Bednarska, J., A. Pelchen-Matthews, …, A. Shevchuk. 2020. Rapid formation of human immunodeficiency virus-like particles. *Proc. Natl. Acad. Sci. USA.* 117:21637–21646. https://doi.org/10.1073/pnas.2008156117.
30. González-Domínguez, I., E. Puente-Massaguer, …, F. Gòdia. 2020. Quantification of the HIV-1 virus-like particle production process by super-resolution imaging: From VLP budding to nanoparticle analysis. *Biotechnol. Bioeng.* 117:1929–1945. https://doi.org/10.1002/bit.27345.
31. Steppert, P., D. Burgstaller, …, A. Jungbauer. 2017. Quantification and characterization of virus-like particles by size-exclusion chromatography and nanoparticle tracking analysis. *J. Chromatogr. A.* 1487:89–99. https://doi.org/10.1016/j.chroma.2016.12.085.
32. Nydegger, S., M. Foti, …, M. Thali. 2003. HIV-1 egress is gated through late endosomal membranes. *Traffic.* 4:902–910.
33. Sackmann, E. K., A. L. Fulton, and D. J. Beebe. 2014. The present and future role of microfluidics in biomedical research. *Nature.* 507:181–189. https://doi.org/10.1038/nature13118.
34. Bruus, H. 2007. Theoretical Microfluidics. Oxford University Press Inc..
35. Fouet, M., M.-A. Mader, …, P. Joseph. 2016. Filter-less submicron hydrodynamic size sorting. *Lab Chip.* 16:720–733.
36. Liot, O., M. Socol, …, P. Joseph. 2018. Transport of nano-objects in narrow channels: influence of Brownian diffusion, confinement and particle nature. *J. Phys. Condens. Matter.* 30:234001. https://doi.org/10.1088/1361-648X/aac0af.
37. Li, N., T. D. Canady, …, B. T. Cunningham. 2021. Photonic resonator interferometric scattering microscopy. *Nat. Commun.* 12:1744. https://doi.org/10.1038/s41467-021-21999-3.
38. Brittain, G. C., 4th, Y. Q. Chen, …, S. Gulnik. 2019. A Novel Semiconductor-Based Flow Cytometer with Enhanced Light-Scatter Sensitivity for the Analysis of Biological Nanoparticles. *Sci. Rep.* 9:16039. https://doi.org/10.1038/s41598-019-52366-4.
39. Renner, T. M., V. A. Tang, …, M. A. Langlois. 2020. Intact Viral Particle Counts Measured by Flow Virometry Provide Insight into the Infectivity and Genome Packaging Efficiency of Moloney Murine Leukemia Virus. *J. Virol.* 94. . e01600-19. https://doi.org/10.1128/JVI.01600-19.

40. Zamora, J. L. R., and H. C. Aguilar. 2018. Flow virometry as a tool to study viruses. *Methods.* 134-135:87–97. https://doi.org/10.1016/j.ymeth.2017.12.011.

41. Pang, Y., H. Song, …, W. Cheng. 2014. Optical trapping of individual human immunodeficiency viruses in culture fluid reveals heterogeneity with single-molecule resolution. *Nat. Nanotechnol.* 9:624–630. https://doi.org/10.1038/nnano.2014.140.

42. Deml, L., C. Speth, …, R. Wagner. 2005. Recombinant HIV-1 Pr55gag virus-like particles: potent stimulators of innate and acquired immune responses. *Mol. Immunol.* 42:259–277. https://doi.org/10.1016/j.molimm.2004.06.028.

43. Briggs, J. A. G., M. N. Simon, …, M. C. Johnson. 2004. The stoichiometry of Gag protein in HIV-1. *Nat. Struct. Mol. Biol.* 11:672–675. https://doi.org/10.1038/nsmb785.

44. González-Domínguez, I., S. Gutiérrez-Granados, …, N. Domingo. 2016. Identification of HIV-1-Based Virus-like Particles by Multifrequency Atomic Force Microscopy. *Biophys. J.* 111:1173–1179. https://doi.org/10.1016/j.bpj.2016.07.046.

45. Timm, A. C., J. W. Warrick, and J. Yin. 2017. Quantitative profiling of innate immune activation by viral infection in single cells. *Integr. Biol.* 9:782–791. https://doi.org/10.1039/c7ib00082k.

46. Liu, W., M. U. Caglar, …, C. E. Cameron. 2019. More than efficacy revealed by single-cell analysis of antiviral therapeutics. *Sci. Adv.* 5:eaax4761. https://doi.org/10.1126/sciadv.aax4761.

47. Chen, H., J. Sun, …, J. Cooper-White. 2015. High-throughput, deterministic single cell trapping and long-term clonal cell culture in microfluidic devices. *Lab Chip.* 15:1072–1083. https://doi.org/10.1039/C4LC01176G.

48. Lin, J., C. Jordi, …, S. Tay. 2019. Ultra-sensitive digital quantification of proteins and mRNA in single cells. *Nat. Commun.* 10:3544. https://doi.org/10.1038/s41467-019-11531-z.

49. Dupire, J., M. Socol, and A. Viallat. 2012. Full dynamics of a red blood cell in shear flow. *Proc. Natl. Acad. Sci. USA.* 109:20808–20813. https://doi.org/10.1073/pnas.1210236109.

50. Szczurek, A. T., K. Prakash, …, U. Birk. 2014. Single molecule localization microscopy of the distribution of chromatin using Hoechst and DAPI fluorescent probes. *Nucleus.* 5:331–340. https://doi.org/10.4161/nucl.29564.

51. Martinac, B., Y. A. Nikolaev, …, C. D. Cox. 2020. Cell membrane mechanics and mechanosensory transduction. *Curr. Top. Membr.* 86:83–141. https://doi.org/10.1016/bs.ctm.2020.08.002.

52. Inamdar, K., F. C. Tsai, …, D. Muriaux. 2021. Full assembly of HIV-1 particles requires assistance of the membrane curvature factor IRSp53. *Elife.* 10:e67321. https://doi.org/10.7554/eLife.67321.

53. Mallucci, L., V. Wells, and M. R. Young. 1972. Effect of trypsin on cell volume and mass. *Nat. New Biol.* 239:53–55. https://doi.org/10.1038/newbio239053a0.

54. Henriques, T., B. S. Scruggs, …, K. Adelman. 2018. Widespread transcriptional pausing and elongation control at enhancers. *Genes Dev.* 32:26–41. https://doi.org/10.1101/gad.309351.117.

55. Tantale, K., E. Garcia-Oliver, …, E. Bertrand. 2021. Stochastic pausing at latent HIV-1 promoters generates transcriptional bursting. *Nat. Commun.* 12:4503. https://doi.org/10.1038/s41467-021-24462-5.

56. Pearson, J. E., P. Krapivsky, and A. S. Perelson. 2011. Stochastic theory of early viral infection: continuous versus burst production of virions. *PLoS Comput. Biol.* 7:e1001058. https://doi.org/10.1371/journal.pcbi.1001058.

57. Cummings, K. W., D. N. Levy, and D. Wodarz. 2012. Increased burst size in multiply infected cells can alter basic virus dynamics. *Biol. Direct.* 7:16. https://doi.org/10.1186/1745-6150-7-16.

58. Timm, A., and J. Yin. 2012. Kinetics of virus production from single cells. *Virology.* 424:11–17. https://doi.org/10.1016/j.virol.2011.12.005.

59. Haase, A. T., K. Henry, …, A. S. Perelson. 1996. Quantitative image analysis of HIV-1 infection in lymphoid tissue. *Science.* 274:985–989. https://doi.org/10.1126/science.274.5289.985.

60. Hockett, R. D., J. M. Kilby, …, R. P. Bucy. 1999. Constant mean viral copy number per infected cell in tissues regardless of high, low, or undetectable plasma HIV RNA. *J. Exp. Med.* 189:1545–1554. https://doi.org/10.1084/jem.189.10.1545.